ARTICLE

Combined Experimental and Theoretical Investigation on the Magnetic Properties Derived from the Coordination of 6-methyl-2-oxonicotinate to 3d-Metal Ions

Laura Razquin-Bobillo,[a] Oier Pajuelo-Corral,[a] Beñat Artetxe,[b] Andoni Zabala-Lekuona,[a] Duane Choquesillo-Lazarte,[c] Antonio Rodríguez-Diéguez,[d] Eider San Sebastian,[a] Javier Cepeda*,[a]

Five new compounds are reported herein starting from 2-hydroxy-6-methylnicotinic acid (H2h6mnic) and first-row transition metal ions, although H2h6mnic shows a prototropy in solution to lead to the 6-methyl-2-oxonicotinate (6m2onic) ligand that is the molecule eventually present in the compounds. The structural and chemical characterization reveals the following chemical formulae: $\{[MnNa(\mu_3\text{-}6m2onic)_2(\mu\text{-}6m2onic)(MeOH)]\cdot H_2O\cdot MeOH\}_n$ ($\mathbf{1_{Mn}}$), $\{[M_2Na_2(\mu_3\text{-}6m2onic)_2(\mu\text{-}6m2onic)_2(\mu\text{-}H_2O)(H_2O)_6](NO_3)_2\}_n$ $[M^{II} = Co$ ($\mathbf{2_{Co}}$) and Ni ($\mathbf{3_{Ni}}$)], $2[Cu_2(6m2onic)_3(\mu\text{-}6m2onic)(MeOH)]\cdot[Cu_2(6m2onic)_2(\mu\text{-}6m2onic)_2]\cdot2[Cu(6m2onic)_2(MeOH)]\cdot32H_2O$ ($\mathbf{4_{Cu}}$) and $\{[Cu(\mu\text{-}6m2onic)_2]\cdot6H_2O\}_n$ ($\mathbf{5_{Cu}}$) (where 6m2onic = 6-methyl-2-oxonicotinate). An unusual structural diversity is observed for the compounds, ranging from isolated complexes (in $\mathbf{4_{Cu}}$), 1D arrays (in $\mathbf{1_{Mn}}$ and $\mathbf{5_{Cu}}$) and 3D frameworks (in $\mathbf{2_{Co}}$ and $\mathbf{3_{Ni}}$). Magnetic properties have been studied for all compounds. Analysis of the magnetic *dc* susceptibility and magnetization data for $\mathbf{4_{Cu}}$ and $\mathbf{5_{Cu}}$ suggests the occurrence of ferromagnetic exchange, which is well explained by broken-symmetry and CASSCF calculations. The sizeable easy-plane magnetic anisotropy present in compound $\mathbf{2_{Co}}$ allows for a field-induced magnet behaviour with an experimental effective energy barrier of 16.2 cm^{-1}, although the slow relaxation seems to be best described through Raman and direct processes in agreement with the results of *ab initio* calculations.

Introduction

The design of coordination polymers (CPs) is a revisited topic that is receiving much attention from many different areas of science owing to the continuous advances shown by these multifunctional materials.[1–3] A key aspect of this success comes from the intriguing architectures and topologies resulting from the careful selection of metal ions and multifunctional ligands, which are self-assembled during the crystallization,[4–6] somehow controlling the final properties of the compound.[7,8] Apart from the potential porosity present in some of these materials, so called metal–organic frameworks (MOFs),[9–11] a wide variety of equally fascinating properties arise from non-porous CPs, such as photoluminescence, conductivity or molecular magnetism.[12–18] With regard to the latter, many efforts have been devoted to understand magnetic exchange and magnetic anisotropy in CPs since it was shown that slow relaxation of the magnetization (SRM) could be extended from single-molecule magnets to these extended systems.[19–22] This new subclass of molecular magnets, belonging to the large group of single-ion magnets (SIMs), consist of only one spin carrier with large magnetic anisotropy and lack of exchange interactions between paramagnetic metal ions along the network.[23] This fact makes them useful for all the potential applications attributed to SMMs, i.e. high-density data storage, quantum computing, and molecular spintronics.[24,25] According to a key concept first postulated by Chang and Long et al. for mononuclear complexes and then postulated by many other works,[26–28] SRM is achieved when the compound possesses ground states with high spin (*S*) and magnetic anisotropy derived from zero-field splitting (*zfs*) *D* and *E* parameters, which stand for the axial and transverse anisotropy, respectively.[29,30] A main characteristic of SIMs is precisely the possibility of imposing substantial magnetic anisotropy by means of a crystal design that leads to a particular coordination geometry and ligand field, a fact that is especially true for 3d transition metal centres owing to the occurrence of unrestricted orbital angular momentum.[31,32] Among them, Co^{II}-based CPs are undoubtedly excellent candidates because of their Kramers nature that reduces the occurrence of quantum tunnelling of magnetization (QTM) relaxation.[33–35] As shown in recent reports,[36–38] the field-induced SIM behaviour, in contrast to traditional SMMs, arises from either easy-axis or easy-plane anisotropy, meaning that *D*

a. Departamento de Química Aplicada, Facultad de Química, Universidad del País Vasco/Euskal Herriko Unibertsitatea (UPV/EHU), 20018 Donostia-San Sebastián, Spain. E-mail: javier.cepeda@ehu.es
b. Departamento de Química Orgánica e Inorgánica, Facultad de Ciencia y Tecnología, Universidad del País Vasco/Euskal Herriko Unibertsitatea (UPV/EHU), 48940, Leioa, Spain.
c. Laboratorio de Estudios Cristalográficos, IACT, CSIC-Universidad de Granada, Avda. de las Palmeras 4, 18100 Armilla, Spain.
d. Departamento de Química Inorgánica, Facultad de Ciencias, Universidad de Granada, 18071 Granada, Spain.

may possess either a negative or a positive value, a phenomenon not fully understood that hence demands further analysis and discussion. Accordingly, investigations accomplishing complete understanding of the electronic states of these sort of compounds are required.

With those ideas in mind, and in a continuous quest for novel ligands able to trigger magnetic properties, the present work is an attempt to explore the potential of the 2-hydroxy-6-methylnicotinic acid (H2h6mnic) ligand to isolate and stabilize the paramagnetic ions. Such ligand contains a hydroxyl and a carboxylate group in strategic adjacent positions, favouring the formation of largely stabilizing chelating rings upon coordination to metals. Importantly, with this arrangement the occurrence of additional links enabling superexchange bridges with neighbouring paramagnetic ions would be prevented. Five compounds of various dimensionalities are described in the present work, combining a tautomer of H2h6mnic and Co(II), Ni(II), Cu(II) and Mn(II) ions. Detailed magnetic studies have been accomplished for all compounds in order to verify the capacity of the ligand to isolate metal centres and prevent undesired magnetic interactions.

Results and Discussion

Previous considerations on H2h6mnic prototropy

The phenomenon of prototropy has been previously described for H2h6mnic when acting as a metal coordinated ligand where the carboxylic group is deprotonated (Scheme 1).[39] This sort of tautomerism, already observed in similar ligands,[40,41] migrates the hydroxyl hydrogen to the pyridinic nitrogen, in such a way that it results in an N–H group, yielding the secondary amine in the newly formed 6-methyl-2-oxonicotinic acid (H6m2onic). The equilibrium seems to be largely shifted to the right even in the absence of metal ions (see Scheme 1) since it is the H6m2onic molecule which is eventually crystallized even if H2h6mnic is dissolved.[39]
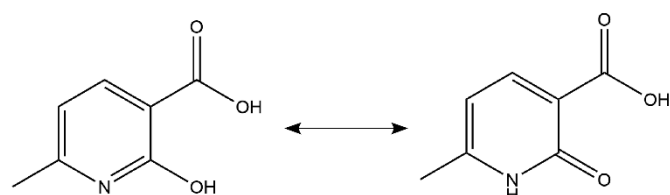
Scheme 1. Prototropic equilibrium of the H2h6mnic molecule (left) to lead to H6m2onic taking place in aqueous solution.

In order to better understand this issue, the geometries of both H2h6mnic and H6m2onic were optimized at DFT level of theory and relative thermodynamic stability compared. These calculations show that the H2h6mnic tautomer is indeed the most stable molecule, being 7 kcal/mol below the energy of H6m2onic (see Figure S29 in the ESI). In any case, such modest energy difference is smaller than the energy of hydrogen bonding interactions (around 15–20 kcal mol^{-1}),[42] which is indicative of a quite homogeneously balanced equilibria in solution, where both tautomers may coexist in similar proportions; such a balance may be broken in the context of crystal network, and therefore, the stabilization of the H6m2onic tautomer against H2h6mnic in the crystalline state is probably related to the establishment of favourable hydrogen bonding

interactions and/or crystallization of the kinetic product. On the one hand, when the molecule is isolated in the free H6m2onic form,[39] a strong intramolecular hydrogen bond is formed between the protonated carboxylic and ketone groups, while the N–H is able to form additional intermolecular hydrogen bonds with the non-protonated carboxylic oxygen atom. On the other hand, when the deprotonated 6m2onic ligand is coordinated to a metal centre, the ketone and adjacent carboxylate groups may form stable chelating rings with the metal ion, leaving the N–H and non-chelating carboxylate oxygen atom available to form hydrogen bonding interactions.

Structural description of compound {[MnNa(μ₃-6m2onic)₂(μ-6m2onic)(MeOH)]·H₂O·MeOH}ₙ (1$_{Mn}$)

Compound **1$_{Mn}$** crystallises in the space-group $P2_1/c$ and its crystal structure contains one-dimensional (1D) metal-organic arrays joined one another into an overall hydrogen-bonded crystal building. The asymmetric unit of the structure consists of one manganese(II) and one sodium(I) metal atom, three 6m2onic ligands, a coordination methanol molecule, together with crystallisation lattice molecules (one water and one methanol). The first metal centre (Mn1) is disposed on a distorted octahedral environment (see continuous shape measures (CShMs), see section 5 in the ESI) formed by the chelating rings from three 6m2onic ligands.[43] The second centre (Na2), also consisting of six oxygen atoms, is formed by five ketone groups of the 6m2onic ligands and an oxygen atom pertaining to the methanol molecule (Figure 1). As it can be seen in Table 1, the Na-O distances are longer than Mn-O distances, in line with the larger ionic radius of sodium, both of them in the usual range found for other Mn(II)- and Na- based CPs.[44–46]
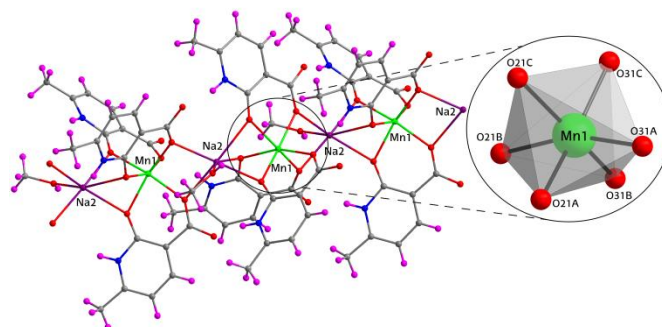
Figure 1. Polymeric structure showing thermal ellipsoids (50% probability) and coordination polyhedron of compound **1$_{Mn}$**. Colour coding: carbon (grey), nitrogen (blue), oxygen (red), hydrogen (pink), manganese (green) and sodium (purple).

Table 1. Selected bond lengths for compound **1$_{Mn}$** (Å).[a]

Coordination sphere of the Mn1 atom			
Mn1–O21A	2.117(3)	Mn1–O31B	2.110(3)
Mn1–O31A	2.150(3)	Mn1-O21C	2.173(3)
Mn1–O21B	2.194(3)	Mn1-O31C	2.124(3)
Coordination sphere of the Na2 atom			
Na2–O21A	2.317(3)	Na2–O21C	2.540(3)

ARTICLE

|			
Na2–O21B	2.577(3)	Na2–O31C(i)	2.437(3)
Na2–O31B(i)	2.328(3)	Na2–O1M	2.348(4)

[a] Symmetries: (i) -x+1/2, y+1/2, -z+1/2.

Two of these ligands use the coordination mode μ_3-$\kappa O21$:$\kappa^2 O21,O31$:$\kappa O31$ to bond to two sodium atoms (in addition to Mn1 atom) by means of the chelating ring. In contrast, the third ligand acquires the μ-$\kappa O21$:$\kappa^2 O21,O31$ binding mode to only one of the two neighbouring sodium atoms. Thanks to these modes, the metal atoms are linked one another to form heterometallic chains running along the crystallographic b axis, where Mn1 and Na2 atoms are sequentially arranged in such a way that the shortest Mn···Mn is of ca. 6.27 Å. In the overall packing, the connection among chains is made by means of hydrogen bonding network in which both the water and methanol molecules are involved. Specifically, in the first hydrogen bonding route connecting adjacent chains, the methanol group attached to the sodium metal binds to the crystallisation methanol molecule, which in turn binds to the crystallisation water molecule that eventually is anchored to two carboxylate oxygen atoms pertaining to the 6m2onic ligands of neighbouring chains (Figure S7). In the second route, the oxygen atom of the carboxylate group that is coordinated to Mn1, acts as hydrogen bonding acceptor of crystallisation water molecule, which is directly bound to the carboxylate group of a 6m2onic ligand of a neighbouring chain.

Structural description of {[M₂Na₂(μ₃-6m2onic)₂(μ-6m2onic)₂(μ-H₂O)(H₂O)₆](NO₃)₂}ₙ [MII = Co (2Co) and Ni (3Ni)].

The heterometallic compounds **2Co** and **3Ni** are isostructural, crystallising in the space-group $I2/a$, so the detailed description of the crystal structure will be made only on the cobalt based compound. **2Co** is an ionic compound that possesses a three-dimensional (3D) cationic framework with nitrate anions occupying the voids. The asymmetric unit of this compound is made up of three metal ions: Co1, Co2 and Na3, among which cobalt atoms present half occupation because they lie on special positions while the sodium atom is disordered into two positions (Na3A and Na3B atoms, which sum up to a whole atom), in such a way that the 1:1 Co:Na ratio is achieved. Additionally, the unit also contains two independent 6m2onic ligands, three and a half coordination water molecules, as well as two disordered nitrate anions. The two cobalt metal centres (Co1 and Co2), located at inversion centres with equivalent donor sets, are coordinated to four oxygen atoms of 6m2onic ligands (through two ketone/carboxylate chelating rings) and two water molecules, in such a way that they exhibit octahedral geometries with low distortion (Figure 2, Table 2). It is worth noticing that water molecules are disordered into two dispositions for Co2 atom (see Figure S8 in the ESI for more details). On its part, the Na3 atom (regarding the dominant contribution of the disordered atom, Na3A) presents a severely distorted six-coordinated environment formed by a chelating carboxylate group, another carboxylate oxygen atom, a ketone oxygen atom and two water molecules, one of which is the bridging μ-OH₂ (O3w) and

the remaining one is disordered into two equivalent positions (O4w, see Figure S9 for more information).
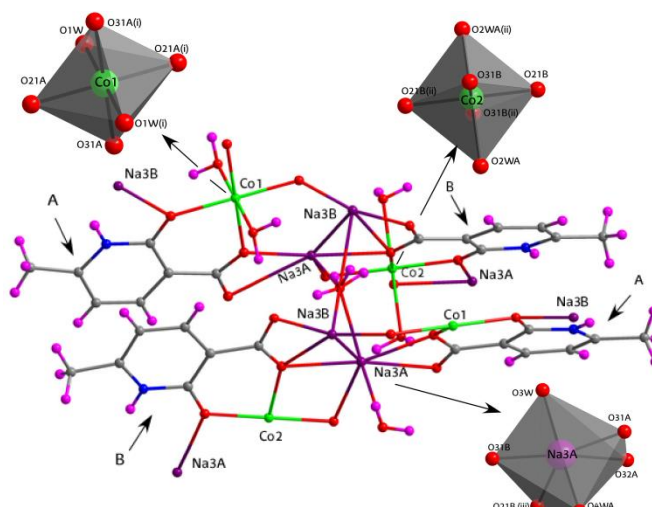
Figure 2. Polymeric structure showing thermal ellipsoids (at 50% probability) and coordination polyhedron of compound **2Co**. Colour coding: carbon (grey), nitrogen (blue), oxygen (red), hydrogen (pink), cobalt (green) and sodium (purple).

Table 2. Selected bond lengths for compound **2Co** (Å).[a] Note that only the dominant contributions of the disordered atoms have been included for better clarity.

Coordination sphere of the Co1 atom			
Co1–O21A	2.053(2)	Co1–O31A(i)	2.025(2)
Co1–O21A(i)	2.053(2)	Co1–O1w	2.164(2)
Co1–O31A	2.025(2)	Co1–O1w(i)	2.164(2)
Coordination sphere of the Co2 atom			
Co2–O21B	2.045(2)	Co2–O31B(ii)	2.024(2)
Co2–O21B(ii)	2.045(2)	Co2–O2wA	2.142(3)
Co2–O31B	2.024(2)	Co2–O2wA(ii)	2.142(3)
Coordination sphere of the Na3 atom			
Na3A–O31A	2.383(2)	Na3A–O31B	2.434(2)
Na3A–O32A	2.889(2)	Na3A–O3w	2.363(2)
Na3A–O21B(iii)	2.486(2)	Na3A–O4wA	2.41(1)

[a] Symmetries: (i) −x−1/2, −y+1/2, −z+1/2; (ii) −x−1, −y, −z; (iii) −x−1, −y+1, −z+1.

The metal centres bind to each other via the bridging 6m2onic and water ligands to form a 3D structure (see Figure S10 in the ESI). Two crystallographically independent 6m2onic ligands, A and B hereafter, are observed. Specifically, ligand A is a tritopic μ_3-6m2onic ligand that joins Na3, Co2 and Na3(v) [where (v) stands for the symmetry: x, -y+1/2, z-1/2] by using the ketone O21 and carboxylate O31 donor atoms. On the other hand, ligand B behaves as a bis-bidentate ligand that simultaneously chelates Co1 and Na3 atoms. While this linking scheme gives rise to a two-dimensional coordination polymer, the O3w

water molecule connects Na3 atoms belonging to adjacent layers.

Structural description of 2[Cu₂(6m2onic)₃(μ-6m2onic)(MeOH)]·[Cu₂(6m2onic)₂(μ-6m2onic)₂]·2[Cu(6m2onic)₂(MeOH)]·32H₂O (4$_{Cu}$)

Compound **4$_{Cu}$** crystallises in the *P*2₁/*c* space group of the monoclinic system and its crystal structure is based on isolated complex entities. In particular, there are three different types of entities: a monomer (Cu1), a centrosymmetric dimer (Cu2 and Cu2(i), see Table 3) and an asymmetric dimer (Cu3 and Cu4).

The monomer consists of two 6m2onic ligands and a methanol molecule. The Cu1 atom is coordinated to five oxygen atoms belonging to two chelating moieties of two independent 6m2onic ligands, which occupy the base of a square pyramidal environment and an oxygen atom of a methanol molecule sited at the apex (Figure 3, see also Table S2 for further information). The d⁹ electronic configuration of the copper(II) atom is known to promote the elongation of the main axis by the Jahn-Teller effect, a fact that is easily observed by checking the coordination distances around Cu1 atom (Table 3).[47–49] In this regard, it must be highlighted that there is a sixth oxygen atom belonging to the carboxylate group of an equivalent 6m2onic ligand at a Cu1···O2A(ii) (ii being the -x+2, -y, -z+1 symmetry) distance of 2.85 Å that would become the monomer into a centrosymmetric dimer, though it has not been considered as a coordination bond. In the centrosymmetric dimer, the symmetrically equivalent Cu2 and Cu2(i) atoms show a square-based pyramid geometry that brings significant differences with respect to Cu1 atom. In particular, while the basal plane is formed by two ketone/carboxylate chelating rings, the oxygen atom in the apical position corresponds to the non-chelating carboxylate oxygen atom (O2C) of a symmetry-related 6m2onic ligand, which sets up the dimeric entity. Finally, the asymmetric dimer contains both situations exhibited in the previous entities. In detail, the Cu3 atom shows a coordination environment similar to that of Cu1 with two chelating rings occupying the base of the pyramid and a MeOH molecule sited in the apical position. In contrast, the Cu4 atom maintains the same O₅ donor set described for Cu2, that is, the fifth atom of the apex being a non-chelating carboxylate oxygen (O1E). In the latter case, a third carboxylate group is located under the base of the pyramidal environment but the Cu3···O2G distance of 2.962 Å (semi-coordination) it is still too long to be considered a coordination bond.
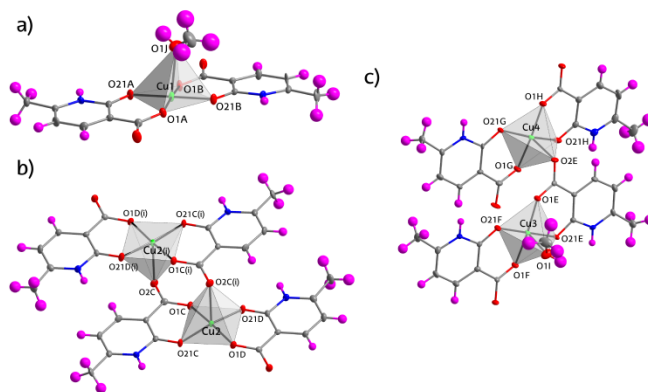
Figure 3. Complex entities of compound **4$_{Cu}$** showing thermal ellipsoids (at 50% probability): **a)** monomeric entity, **b)** centrosymmetric dimeric entity and **c)** asymmetric dimeric entity. Colour coding: carbon (grey), nitrogen (blue), oxygen (red), hydrogen (pink) and copper (green).

Table 3. Selected bond lengths for compound **4$_{Cu}$** (Å).[a]

Coordination sphere of the Cu1 atom			
Cu1–O1A	1.928(2)	Cu1–O21B	1.940(2)
Cu1–O21A	1.925(2)	Cu1–O1J	2.406(3)
Cu1–O1B	1.934(2)		

Coordination sphere of the Cu2 atom			
Cu2–O1C	1.923(3)	Cu2–O1C(i)	1.923(3)
Cu2–O2C	2.444(2)	Cu2–O2C(i)	2.444(2)
Cu2–O21C	1.924(3)	Cu2–O21C(i)	1.924(3)
Cu2–O1D	1.922(3)	Cu2–O1D(i)	1.922(3)
Cu2–O21D	1.914(3)	Cu2–O21D(i)	1.914(3)

Coordination sphere of the Cu3 atom			
Cu3–O1E	1.925(2)	Cu3–O21F	1.926(2)
Cu3–O21E	1.924(2)	Cu3–O1I	2.380(3)
Cu3–O1F	1.936(2)		

Coordination sphere of the Cu4 atom			
Cu4–O2E	2.362(2)	Cu4–O1H	1.922(2)
Cu4–O1G	1.926(2)	Cu4–O21H	1.935(2)
Cu4–O21G	1.926(2)		

[a] Symmetries: i) –x+1, –y+1, –z+1.

The isolated entities are stabilised and linked along the crystal building by an intricate supramolecular network of hydrogen bonds, in which water molecules play a key role. Taking into account that the compound possesses 32 crystallisation solvent molecules per chemical formula, the hydrogen bonds will not be described herein for the sake of simplicity. In any case, their role can be summarised by stating that they act as acceptors with MeOH (O–H) and pyridine (N–H) groups, and as donors with carboxylate/ketone groups, while they also conform some infinite hydrogen-bonding clusters.

Structural description of {[Cu(μ-6m2onic)$_2$]·6H$_2$O}$_n$ (5$_{Cu}$).

Compound **5$_{Cu}$** crystallizes in the *P*2$_1$/*c* space group and consists of copper(II)-6m2onic chains and crystallisation water molecules held together by hydrogen bonding interactions. The asymmetric unit of this compound consists of a copper atom (Cu1), a 6m2onic ligand and three lattice water molecules. Although this content does not a priori meet the title chemical formula of the compound, it should be noted that Cu1 atom has half occupancy in the structure because it is sited on the screw axis, whereas the ligand and the three water molecules occupy general positions. The copper(II) centre is coordinated to six oxygen atoms giving rise to an octahedral environment (Table 4, see CShMs in the ESI). The six oxygen atoms come from four symmetry related 6m2onic ligands, four of which correspond to ketone/carboxylate oxygen atoms establishing chelating rings that occupy the equatorial plane, whereas the remaining two oxygen atoms occupying the main axis belong to other two carboxylate groups (Figure 4). In this sense, the 6m2onic ligand shows the same μ-κ^2*O,O'*:κ*O''* coordination mode exhibited by the bridging ligands in the centrosymmetric dimeric entity of compound **4$_{Cu}$** (see Figure 3b). As all the ligands act as bridges between adjacent Cu1 atoms (Cu···Cu distances of ca. 5.14 Å), infinite metal-organic chains are generated along the crystallographic [100] direction.

Table 4. Selected bond lengths for compound **5$_{Cu}$** (Å).[a]

Cu1–O21A	1.924(3)	Cu1–O21A(i)	1.924(3)
Cu1–O31A	1.931(2)	Cu1–O31A(i)	1.931(2)
Cu1–O32A(ii)	2.680(3)	Cu1–O32A(iii)	2.680(3)

[a] Symmetries: i) –x+2, –y, –z+1; ii) –x+1, –y+1, –z+2; iii) x+1,y,z.
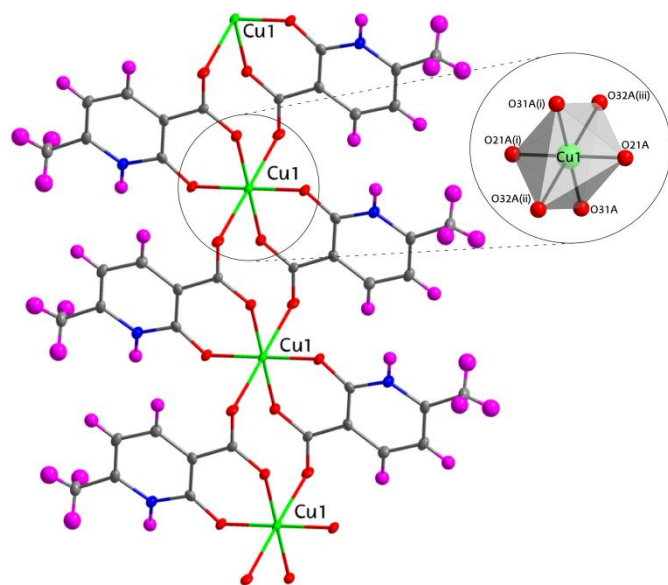
Figure 4. Polymeric structure showing thermal ellipsoids (at 50% probability) and coordination polyhedron of compound **5$_{Cu}$**. Colour coding: carbon (grey), nitrogen (blue), oxygen (red), hydrogen (pink) and copper (green).

The junction among the chains in the crystal packing occurs via hydrogen bonds mediated by the crystallisation water molecules. In particular, a detailed analysis of these interactions reveals that they form two-dimensional water clusters that may be named as L8(2)8(4) layers (see Figure S11).[50]

## Magnetic measurements

Static magnetic properties

As mentioned in the structural description, the paramagnetic metal centres of most of these compounds are practically isolated (well separated from each other) in the crystal building except for the Cu(II)-based compounds, which contain short (ca. 5.0 Å) ligand mediated bridges that could lead to magnetic exchange. Therefore, with the aim of investigating the magnetic anisotropy of the Mn(II)-, Ni(II)- and Co(II)-based compounds for their potential slow magnetic relaxation,[51–53] and the magnetic exchange in Cu(II)-based compounds, the analyses of the temperature-dependent (2–300 K) magnetic susceptibility measurements were accomplished for all compounds over polycrystalline samples under a *dc* field of 1000 Oe. Starting from compound **1$_{Mn}$**, the room temperature value of the $\chi_M T$ product is 4.88 cm^3 K mol^{-1}, slightly higher than the expected for an uncoupled high spin Mn(II) ion with *g* = 2.00 (4.38 cm^3 K mol^{-1}). This value remains practically constant cooling down to 30 K, below which it experiments a deep fall to reach a value of 4.68 cm^3 K mol^{-1} at 2K (see Figure S13 in the ESI). This behaviour may be attributed to a small *zfs* because Mn(II) atoms are quite isolated from each other in the crystal structure (the minimum Mn···Mn is of 6.27 Å), in such a way that antiferromagnetic exchange is to be discarded. Magnetization measurements carried out in the 0–7 T region for the 2–7 K temperatures present the typical curves for an uncoupled centre, describing a plateau at 2 K with a value close to saturation (5.3 Nβ ≈ 5.0 Nβ). $\chi_M T$ vs *T* and *M* vs *H* data were simultaneously fitted using PHI program[54] by using the spin Hamiltonian of equation 1:

$$\hat{H} = D(\hat{S}_z^2 - \hat{S}/3) + E(\hat{S}_x^2 + \hat{S}_y^2) + \mu_B H g \hat{S} \text{ (eq. 1)}$$

where all the parameters have their usual meaning. The best fitting of the data gave the following set of results: *D* = -0.26(4) cm^{-1}, *E* = 0.08(1) cm^{-1} and *g*= 2.10(1), thus concluding that compound **1$_{Mn}$** possesses a very small but non negligible magnetic anisotropy as expected from previous magneto-structural correlations.[51] On the other hand, the analysis of the magnetic data for compound **3$_{Ni}$** showed that $\chi_M T$ at room temperature (1.51 cm^3 K mol^{-1}) is significantly higher than the corresponding spin-only value (*S* = 1, $\chi_M T_{300K}$ = 1.00 cm^3 K mol^{-1}). Similarly to compound **1$_{Mn}$**, the $\chi_M T$ product of **3$_{Ni}$** presents a large plateau down to 40 K, and then it subtly decreases to a value of 0.57 cm^3 K mol^{-1} at 2K (Figure S14). The magnetization curves measured for the 2–7 K range show a linear increase up to 3.5 T followed by a smoother rise at higher fields to reach a value of 2.03 Nβ. Attempts to simultaneously fitting the susceptibility and all magnetization curves failed to converge

but an optimum fitting was achieved by fitting $\chi_M T$ vs T and M vs H at 2 K, from which the set: $D = +12.00(1)$ cm^{-1}, $E = 4.60(1)$ cm^{-1} and $g = 2.37(2)$ was estimated. The large rhombicity is consistent with the magnetostructural relationships estimated for other Ni(II)-based compounds.[30]

With regard to compounds **4$_{Cu}$** and **5$_{Cu}$**, both of them exhibit a similar magnetic behaviour owing to the fact that, aside from small structural distortions, they share double carboxylate mediated μ-κO:κO bridges acting as superexchange pathway between copper(II) ions (Figure 5).
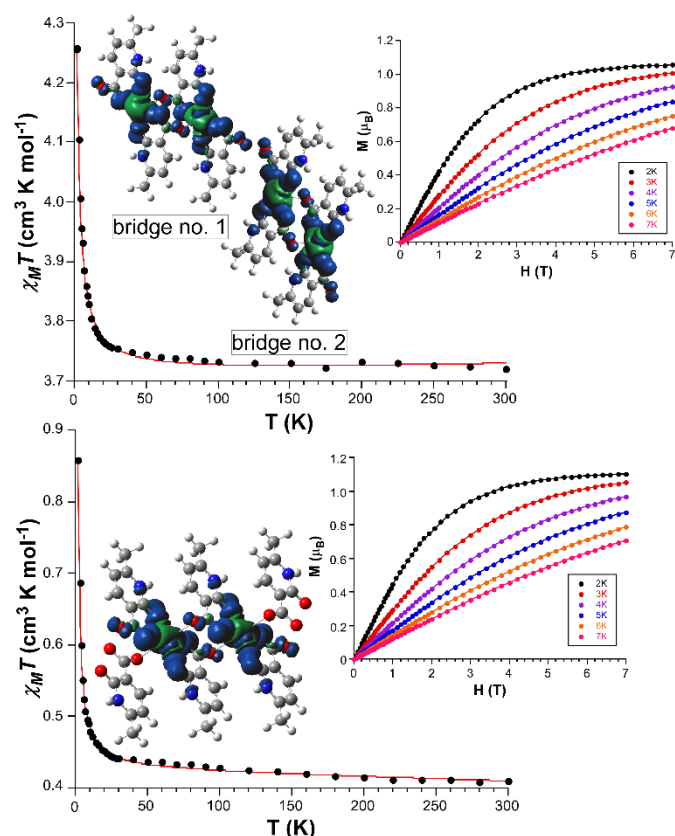
Figure 5. $\chi_M T$ vs T plots of compounds **4$_{Cu}$** (top) and **5$_{Cu}$** (bottom) showing the best fit according to eq. 2. Insets in both plots show the spin density around the paramagnetic atoms as well as the fitted magnetization curves at variable temperature.

The magnetic behaviour of these compounds in the form of $\chi_M T$ vs T plots presents a very similar behaviour, showing a very slight increase upon cooling down from room temperature to 50 K, below which it experiments a steep increase. Considering that compound **4$_{Cu}$** contains a total of eight Cu(II) ions per formula unit and that only one describes the formula of **5$_{Cu}$**, the room temperature values of $\chi_M T$ (3.71 and 0.41 cm^3 K mol^{-1}) can be considered slightly greater than the calculated for an uncoupled spin doublet (0.375 cm^3 K mol^{-1}). The $\chi_M T$ product reaches a value of 4.21 and 0.85 cm^3 K mol^{-1} at 2 K, respectively for **4$_{Cu}$** and **5$_{Cu}$**, which indicates the occurrence of weak ferromagnetic interactions. This fact is in agreement with the magnetization vs field curves recorded in the 2–7 K range for both compounds. In these plots, especially at 2K, magnetization shows a quite rapid increase to reach saturation at ca. 4 T with values close to 1 Nβ. In order to evaluate the magnitude of the exchange interactions as well as

zfs and g parameters, a combined fitting of the susceptibility and magnetization curves was performed with PHI program (see equation 2). The best fitting results by means of least-squares analysis for **4$_{Cu}$** and **5$_{Cu}$** are $J = +0.71(2)$ cm^{-1}, $g = 2.13(1)$ and $|D| = 0.67(1)$ cm^{-1}, with R = 5.7 x 10^{-3} for **4$_{Cu}$** and $J = +0.82(2)$ cm^{-1}, $g = 2.20(1)$ and $|D| = 0.83(1)$ cm^{-1}, with R = 3.3 x 10^{-3} for **5$_{Cu}$**.

$$\hat{H} = -JS_1 \cdot S_2 + S_1 D S_2 + \mu_B H g \hat{S} \text{ (eq. 2)}$$

A main conclusion derived from this analysis is the fact that the zero-field splitting of the ground triplet state (D value) is greater for **5$_{Cu}$** than that of **4$_{Cu}$**, in agreement with the larger distortion of the coordination polyhedron (significantly distorted octahedron in **5$_{Cu}$** and slightly distorted square-based pyramid in **4$_{Cu}$**, see Table S2 in the ESI), a fact that has been previously observed.[55]

To get deeper insights into the magnetic properties of these compounds, we computed the value of J for the three similar double carboxylate mediated superexchange pathways present in these compounds: i) in the centrosymmetric dimeric entity, ii) in the asymmetric dimeric entity, iii) in the $[Cu_2(CO_2)_2]_n$ units of the chain. In all cases, the results derived from the broken-symmetry methodology through DFT theory based on the $\hat{H}$ (HDvV) = $-JS_1 \cdot S_2$ spin-Hamiltonian gave positive and small values of the exchange constant confirming a ferromagnetic coupling (Table 5).

Table 5. Main results from the computed J values for compounds **4$_{Cu}$** and **5$_{Cu}$**.

Compound	Exp.	BS - DFT	CASSCF(2,2)	
	J (cm^{-1})	J (cm^{-1})	G.S.	J (cm^{-1})
4$_{Cu}$				
centr. dimer (bridge 1)	0.71	0.89	*Mult.* = 3	0.1
asym. dimer (bridge 2)		0.46	*Mult.* = 3	0.0
5$_{Cu}$				
$[Cu_2(CO_2)_2]_n$ excerpt	0.82	0.65	*Mult.* = 3	0.2

In an alternative way, the coupling constant was also estimated through the calculation of the energy gap between the triplet-singlet by using CASSCF calculations based on metal-only active space. Accordingly, an active space composed of two 3d orbitals of the Cu(II) ions was constructed for the multireference calculations based on the previously employed dimeric models. Note that localized orbitals were used for an easier interpretation and assignation. The CAS(2,2) calculations give a Heisenberg ordering of the states that ranks, in all cases, the ferromagnetic $S = 1$ as the ground state, with the $S = 0$ state sited around 0.1 cm^{-1} above in energy. Therefore, it can be concluded that this second methodology, yet valid to predict the nature of the magnetic coupling, clearly underestimates the magnitude of the exchange as previously observed for other complexes.[56] As expected for square-based pyramid and axially elongated octahedral environments (present in **4$_{Cu}$** and **5$_{Cu}$**, respectively), the unpaired electrons reside on the $d_{x^2-y^2}$ orbital, which is confirmed by the spin

density surfaces (see Figure 5). As a result, the spin density in the main axis of both polyhedra is scarce, making the overlap between magnetic orbitals of the copper(II) ions within the equatorial-axial carboxylate superexchange pathway to be poor and hence, it brings a weak antiferromagnetic contribution and a dominant ferromagnetic behaviour to the compounds. Such weak ferromagnetic behaviour has been documented for other ligands with similar carboxylate bridges.[57–59]

With regard to compound **2$_{Co}$**, it must be mentioned that it possesses two symmetry independent cobalt(II) atoms (Co1 and Co2) with identical chemical donor sets and practically equal structural environments, so only one paramagnetic centre will be considered for the sake of simplicity. At room temperature, the $\chi_M T$ value of compound **2$_{co}$** is of ca. 2.8 cm^3 K mol^{-1} per Co(II) atom, a significantly higher value than the expected for an octahedral Co(II) ion (g = 2.01, spin-only value is 1.87 cm^3 K mol^{-1}), which suggests the presence of an unquenched first order spin-orbit coupling (SOC) of the $^4T_{1g}$ ground state for a high spin octahedral environment. The solid-state diffuse reflectance spectrum agrees with the usual d-d transition of high-spin Co^{II} in distorted octahedral geometry, showing a first wide and not resolved band at about 640 nm that is assigned to the $^4T_{1g}(F) \rightarrow {}^4A_{2g}(F)$ transition followed by two overlapped bands in the 440–580 nm range that are assigned to the $^4T_{1g}(F) \rightarrow {}^4T_{1g}(P)$ transitions.[53] The strongly absorbing bands below 400 nm are derived from charge transfer transitions and intraligand transitions (see Figure S12 in the ESI). Upon cooling, the $\chi_M T$ value remains almost constant down to 150 K, below which it experiments a gradual decrease, mainly below 30 K, to reach a value of 1.86 cm^3 K mol^{-1} at 2 K (Figure 6). In addition to the first order SOC effect usually present in Co(II) distorted octahedra,[3,4] the low temperature drop in the magnetic susceptibility may be also attributed to the contribution of weak antiferromagnetic interactions. As observed in Figure S15, the χ_M^{-1} vs. T curve follows the Curie-Weiss law in the 50-300 K temperature range with C = 2.91 cm^3 K mol^{-1} and ϑ = -10.01, which is mainly due to the orbital contribution of Co(II) centre. According to the SOC present in compound **2$_{Co}$**, the equation proposed by Rueff and co-workers[60] (equation 3) was employed to estimate the anti-ferromagnetic exchange interactions:

$$\chi_M T = A \, exp(-E_1/kT) + B \, exp(-E_2/kT) \text{ (eq. 3)}$$

where A and B parameters correspond to the sum of the Curie constant and E_1 and E_2 represent the "activation energies" of spin-orbit coupling and antiferromagnetic exchange interactions, respectively. Best fitting results were obtained for the dataset: A = 0.89(1), B = 2.08(1) ($A+B$ = 2.9 cm^3 K mol^{-1}), E_1/κ = +33.52 and $-E_2/\kappa$ = -0.10, which fall in the range found for other Co(II) compounds.[61] This small value calculated for E_2 suggests that the anti-ferromagnetic interactions among Co(II) ions are very weak, in agreement with the large shortest Co···Co distances found in the crystal structure (ca. 7.0 Å between Co1 and Co2). In order to further explore the SOC present in the compound, the experimental $\chi_M T$ vs T curve was

fitted using the PHI program on the basis of the following Hamiltonian (equation 4):[62]

$$\hat{H} = \sigma\lambda(L_{Co}S_{Co}) + \Delta[L_{z,Co}{}^2 - L_{Co}(L_{Co}+1)/3] + \mu_B H \cdot (-\sigma L_{Co} + g S_{Co}) \text{ (eq. 4)}$$

where λ corresponds to the SOC parameter, Δ equals the energy gap between $^4A_2$ and ^4E levels derived from the axial orbital splitting of the $^4T_{1g}$ ground state, and σ represents the orbital reduction factor defined as σ = -Aκ (with A being the admixture of the upper $^4T_{1g}$ (^4P) state into the $^4T_{1g}$ (^4F) ground state and κ the reduction of the orbital momentum). The obtained parameters according to PHI code fit quite well the experimental data (Figure S17) with λ = -89(2) cm^{-1}, Δ = 16(2) cm^{-1}, σ = -0.38(1) and g = 2.49(1). It is worth noticing that no reliable fitting was achieved when introducing anisotropic components for the gyromagnetic parameter.
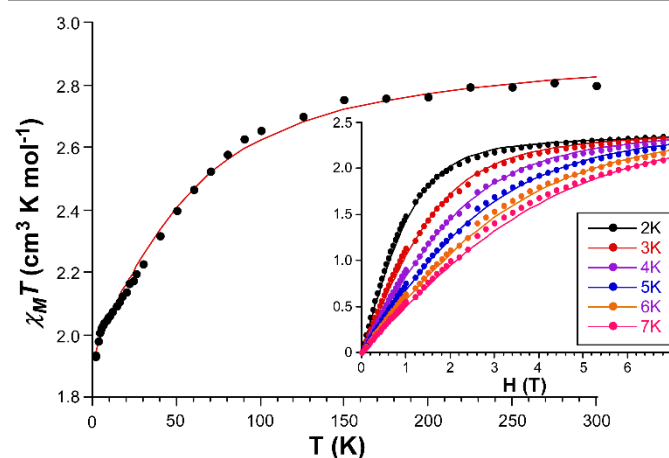

Figure 6. Simultaneous best fit of $\chi_M T$ vs T and M vs H plots using eq. 1 for compound **2$_{co}$**.

Taking into account the large value of Δ, it was assumed that only the two lowest Kramers doublets (KDs) of the $^4A_2$ ground state are thermally populated, meaning that their energy gap equals to the axial zfs within the quartet state, in such a way that the magnetic properties can be derived from the following spin Hamiltonian of equation 1. The isothermal M vs H curves collected between 0 and 7 T in the 2-7 K temperature range do not reach the theoretical saturation for S = 3/2 (M$_{sat}$ = 3.3, with g = 2.2, see inset in Figure 6). The latter, in addition to the fact that reduced magnetization curves do not collapse in a single master curve (see Figure S18), supports the presence of significant magnetic anisotropy. Best fitting using both, susceptibility and magnetization data by PHI program gives D = +25(1) cm^{-1}, E = 8.0(1) and g = 2.48(1) with R = 2.4 x 10^{-2}, which are in line with most of previously reported six-connected Co(II) based complexes.[35] In any case, in order to justify the sign of D parameter, magnetization and susceptibility data were additionally calculated by initializing the fitting process with a negative D, which led the following set of parameters and a much poorer fit: D = -28(1) cm^{-1}, E = -0.5(9) and g = 2.48(1). The positive sign of D value in addition to the large value of E indicates an easy plane magnetic anisotropy governing the magnetic properties of compound **2$_{Co}$**, a fact that has been commonly observed in slightly distorted Co(II) octahedral compounds.[63,64] As a consequence

of such positive sign, the $m_s = \pm 1/2$ doublet is below the $m_s = \pm 3/2$ doublet.

Dynamic magnetic properties

Alternating current (*ac*) magnetic susceptibility measurements were conducted on compounds **1$_{Mn}$**, **2$_{Co}$** and **3$_{Ni}$** in view of the magnetic anisotropy shown. To start with, the curves were recorded under an oscillating field of 3.5 Oe as well as no applied *dc* field, finding no maximum in the out-of phase (χ'') signal even for the curve recorded at the maximum frequency (see ESI). This fact seems to indicate that the compounds present fast quantum tunnelling of the magnetization effect (QTM). The application of an external *dc* field of 1000 Oe only showed the occurrence of maxima in compound **2$_{Co}$**, preventing any further analysis in compounds **1$_{Mn}$** and **3$_{Ni}$**. In **2$_{Co}$**, a nice set of frequency dependent maxima are observed in the 2-4.5 K range. This fact confirms the occurrence of SMM behaviour (Figure 7). As observed, all the curves (except for those acquired for the lowest frequencies of 60 and 200 Hz) present a descending tail below the temperature of the maximum, which indicates the absence of QTM. The Cole-Cole plots for the 2.9-4.5 K range present regular semi-circular shapes and thus, they have been fitted with the generalized Debye model, from which α values ranging between 0.07 and 0.28 (indicative of the coexistence of several relaxation mechanisms) are obtained. In fact, a somewhat curvilinear distribution is found when plotting the temperature dependent distribution of the relaxation times in the form of ln(τ) vs 1/T. In a rough approximation, the data can be fitted to the Arrhenius law (equation 5) in the high temperature region (3.5–4.5 K), obtaining an energy barrier for the reversal of the magnetization (U_{eff}) of 23.3 K and a τ_0 of 9.32 x 10^{-8} s. These values fall within the habitual ones estimated for Co(II)-based CPs with SMM behaviour (1 x 10^{-7} – 1 x 10^{-11} s).[31]

$$\tau^{-1} = \tau_0^{-1} \exp(U_{eff}/\kappa_B T) \quad \text{(eq. 5)}$$

To better reproduce the whole temperature dependent relaxation times of the compound, these data were fitted to the occurrence of simultaneous relaxation through direct and Raman mechanisms, for which equation 6:

$$\tau^{-1} = A_{direct} T + B_{Raman} T^n \quad \text{(eq. 6)}$$

In this way, the fitting fairly reproduces the curve with the following set of values for the parameters: A_{direct} = 707 s^{-1} K^{-1}, B_{Raman} = 4.43 s^{-1} K^{-n} with n = 6.0 (a value that can be considered as reasonable according to the bibliography).[63,65,66] To end with this section, it must be highlighted that the inclusion of the QTM did not improve the fitting at all, which suggests that this mechanism is not important in the present relaxation scenario in line with, as above mentioned, the shape of the field-induced χ'' curves.
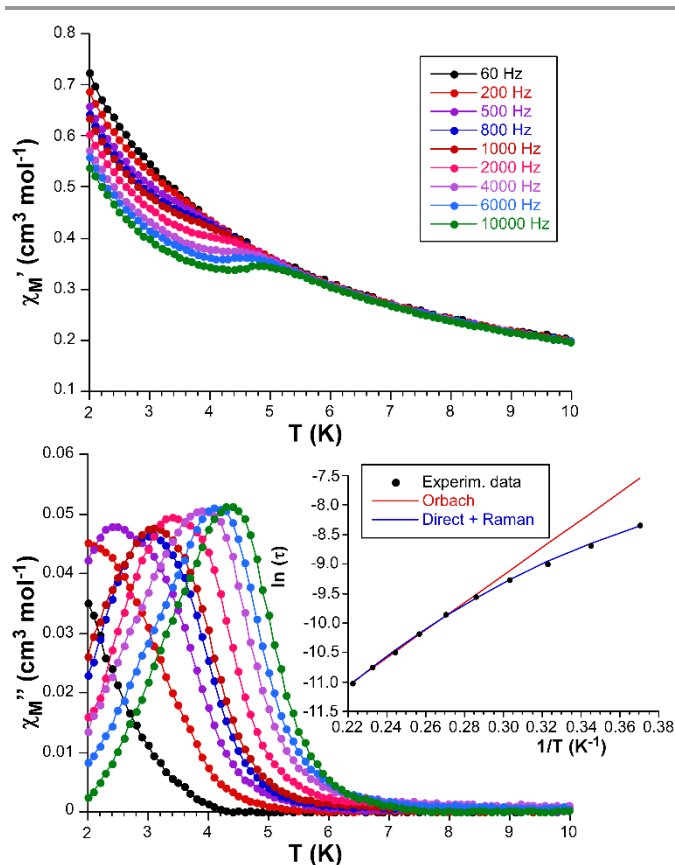

Figure 7. Temperature dependence of the **(a)** χ_M' signals and **(b)** χ_M'' signals for compound **2$_{Co}$** under an applied field of 1000 Oe. Inset shows the temperature dependence for the relaxation times and best fits of the data to different relaxation processes.

Ab initio calculations

Ab initio multireference calculations were performed with ORCA 5.0.2 software package in order to get a deeper insight into the magnetic properties of the compounds. However, taking into account that SMM behaviour is only observed for **2$_{Co}$**, only a detailed analysis is provided herein for the latter (see ESI for further details on compounds **1$_{Mn}$** and **3$_{Ni}$**). The appropriate model of this compound was achieved by optimizing the hydrogen atoms of the 6m2onic and water ligands of the coordination excerpt of Co1 atom (see computational details for further information), because equivalent models grown directly from the X-ray coordinates nor from fully optimized molecule did not correctly represent the nature and sign of many magnetic parameters. Moreover, it is worth mentioning that very similar results were obtained for the equivalent model grown around the Co2 centre, so only Co1 is detailed herein. To start with, the CASSCF/NEVPT2 calculations gave a correct interpretation of the *zfs* parameters of the compound since both the sign of the computed *D* value and the *E/D* ratio were in agreement with the experimental results (values of *D* = +25 with *E/D* = 0.32 were achieved experimentally), although the theoretical magnitudes are clearly overestimated (Table 6).

Table 6. NEVPT2 results calculated on the H-optimized structure of compound **2$_{Co}$**.[a]

D (D_{KD1-2}, D_{KD1-3})[b]	+74.1 (+42.9, +20.8)
E/D	0.32
g_{xx}, g_{yy}, g_{zz}	1.93, 2.40, 2.92
g_{iso}	2.42
ΔE (1-2), ΔE (1-3)[c]	198.1, 765.8

[a] The energy values are given in cm^{-1}. [b] The two values in the parentheses after D represent the contribution to D form the ground to first and ground to second exited state transitions, respectively. [c] The energy separation between KDs.

The electronic configuration of the ground state is strongly multideterminantal, with a main $(d_{yz})^2(d_{xz})^2(d_{xy})^1(d_{x^2-y^2})^1(d_{z^2})^1$ configuration (48%) as well as other significant contributions with low weightage (of ca. 15%, see Figure S28 in the ESI). This fact is expected for the unquenched orbital contribution present in the six-coordinate Co(II) environment that usually leads to large values of D, as found in other complexes.[34,67] The major contribution to D and E parameters comes from the two lowest lying excited states, which are almost monodeterminantal in nature with main $(d_{yz})^2(d_{xz})^1(d_{xy})^2(d_{x^2-y^2})^1(d_{z^2})^1$ and $(d_{yz})^1(d_{xz})^2(d_{xy})^2(d_{x^2-y^2})^1(d_{z^2})^1$ configurations, meaning that the main excitations contributing to the *zfs* parameters correspond to $d_{xz} \rightarrow d_{xy}$ and $d_{yz} \rightarrow d_{xy}$ (Figure 8). The fact that the orbitals involved in the magnetic anisotropy have distinct m_l levels explains well the positive sign of D parameter,[68] which is also supported by the d orbital splitting from the ab initio ligand field theory (AILFT) approach.[69]

Additionally, the energy of the three lowest-lying KDs were computed with the SINGLE_ANISO code as implemented in ORCA.[70,71] Based on these calculations, the first excited state lies 194 cm^{-1} above the ground state, making such a large blocking barrier to be much greater than the experimentally estimated from *ac* susceptibility measurements (U_{eff} of 16.2 cm^{-1}). In line with the matrix elements plotted in Figure 8b, the Orbach process is not applicable for the present case as the direct relaxation between the ground $M_s = \pm 1/2$ state is operative and the first excited KD is comparatively far in energy (at ca. 200 cm^{-1}). Therefore, it seems reasonable to say that other relaxation pathways such as Raman and direct processes must be more important for the reversal of the magnetization for this compound. In any case, QTM may be somewhat relevant in view of the relatively high coefficient (0.7 μ_B), which explains the complete quenching of the slow relaxation of the magnetization under zero *dc* field.
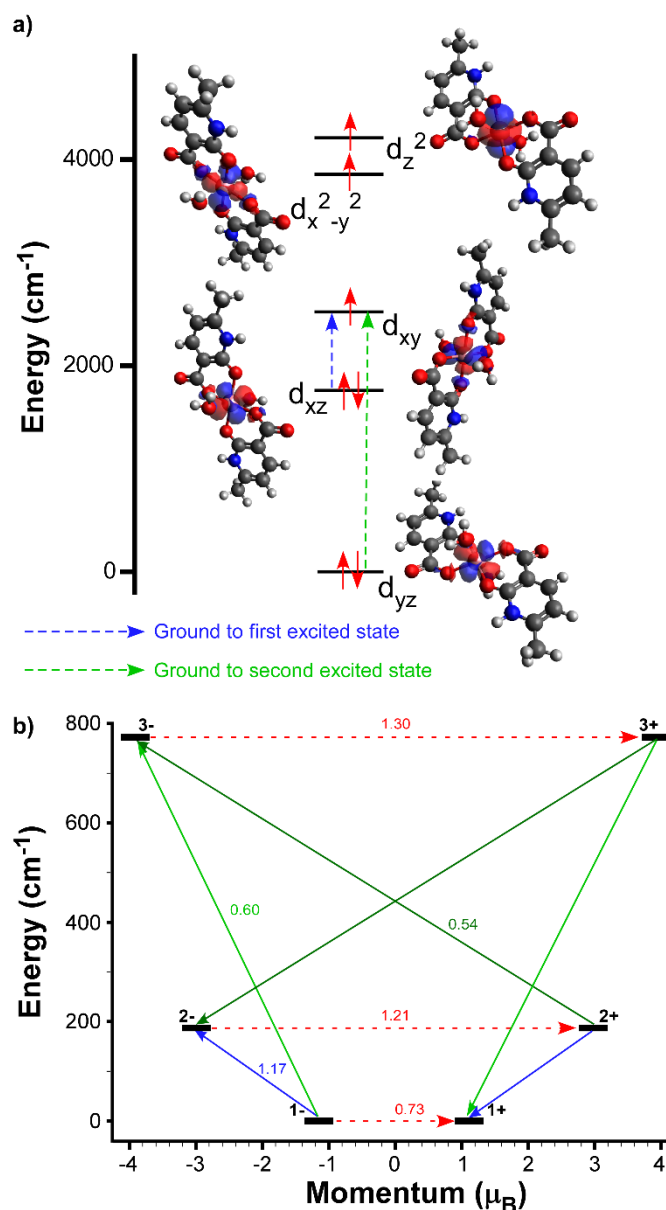
Figure 8. a) AILFT computed d-orbital splitting and **b)** *Ab initio* computed relaxation mechanism with three lowest KDs of compound **2$_{Co}$**. Blue lines indicate the probable relaxation pathways for magnetization reversal mechanism and green lines show the less possible pathways through excited states. The dotted red lines represents the ground state QTM and TA-QTM (thermally assisted-QTM) via first and second excited KDs. The numbers close to each arrow designate matrix elements of transition magnetic moments.

Conclusions

2-hydroxy-6-methylnicotinic acid (2h6mnic) undergoes prototropy in aqueous solution and, in the presence of first row metal ions such as Cu(II), Mn(II), Co(II) and Ni(II), the 6m2onic tautomer is stabilized when coordinated to the metal centre. This fact brings the formation of a preponderant chelating ring by means of the adjacent ketone/carboxylate groups that rules the coordination to all studied divalent metal ions, despite of which it gives slightly different coordination patterns that eventually yield a variety of crystal structures. Briefly, a supramolecular building composed of adimensional complexes and a 1D double laddered coordination polymer

(CP) are formed with Cu(II), an heterometallic 1D CP is achieved with Mn(II) and Na(I) and two isostructural 3D cationic frameworks are obtained with Co(II) or Ni(II) and Na(I) ions. The analysis of the magnetic properties reveals the occurrence of very weak ferromagnetic exchange interactions ($J < 1$ cm^{-1}) in the copper-based compounds, in which the coupling takes place through carboxylate mediated μ-κO:κO bridges. Computational calculations confirm the weak ferromagnetic coupling between adjacent metal ions. On its part, the cobalt-based 3D CP is composed of isolated spin carriers owing to the presence of sodium ions completing the secondary coordination sphere, as it is evidenced by the experimental magnetic *dc* data. Interestingly, the slightly distorted octahedral CoO$_6$ centres present in the compound are denoted, as suggested by best fitting results of the susceptibility and magnetization curves, with an easy-plane magnetic anisotropy with large rhombicity. *Ab initio* CASSCF/NEVPT2 calculations point in the same direction giving substantially overestimated *D* and *E* parameters, although the same *E/D* ratio is observed. Moreover, they show that d$_{xz}$ → d$_{xy}$ and d$_{yz}$ → d$_{xy}$ are the main excitations contributing to the *zfs* parameters. The compound presents a field-induced single-molecule magnet behaviour according to *ac* susceptibility data, where the magnetic relaxation is best described by means of Raman and direct processes. These results are in agreement with *ab initio* calculations, which predict a higher blocking barrier than that estimated from experimental Arrhenius law (*U*$_{eff}$ of 194 vs 16.2 cm^{-1}) while the probabilities rendered by matrix transition elements allow for the occurrence of the mentioned processes.

Experimental Section

Chemicals. All chemicals were of reagent grade and were used as commercially obtained with any further purification.

Synthesis of {[MnNa(μ_3-6m2onic)$_2$(μ-6m2onic)(MeOH)]·H2O·MeOH}$_n$ (1$_{Mn}$). 0.0613 g of H2h6mnic (0.4 mmol) were placed in a scintillation vial and dissolved in 10 mL of methanol (MeOH). 0.0502 g of Mn(NO$_3$)$_2$·4H$_2$O (0.2 mmol) were dissolved in 2 mL of distilled water and added dropwise to the previous solution. Then, to the resulting aqueous-methanol solution 0.2 mmol of NaOH (added in the form of a 1 M aqueous solution) were added, in such a way that a yellowish precipitate was formed. The precipitate was filtered off and the resulting solution was left to slowly evaporate at room temperature. 3 days later, light yellow single crystals of 1$_{Mn}$ were observed and collected by filtration, after which they were washed with MeOH. Yield (based on metal): 50%. Anal. Calcd for C$_{23}$H$_{28}$MnN$_3$NaO$_{12}$ (%): C, 44.82; H, 4.58; N, 6.82. Found: C, 44.53; H, 4.75; N, 6.68.

Synthesis of {[M$_2$Na$_2$(μ_3-6m2onic)$_2$(μ-6m2onic)$_2$(μ-H$_2$O)(H$_2$O)$_6$](NO$_3$)$_2$}$_n$ [M = Co (2$_{Co}$) and Ni (3$_{Ni}$)]. The same procedure was followed replacing Mn(NO$_3$)$_2$·4H$_2$O by Co(NO$_3$)$_2$·6H$_2$O or Ni(NO$_3$)$_2$·6H$_2$O in the mixture. The slow evaporation of the filtered solutions gave red and green single crystals that were washed with MeOH. Yields of 45 and 50% based on metal. Anal. Calcd for C$_{28}$H$_{38}$Co$_2$N$_6$Na$_2$O$_{25}$ (%): C,

32.89; H, 3.75; N, 8.22. Found: C, 33.03; H, 3.52; N, 8.35. Anal. Calcd for C$_{28}$H$_{38}$N$_6$Ni$_2$Na$_2$O$_{25}$ (%): C, 32.91; H, 3.75; N, 8.22. Found: C, 32.81; H, 3.65; N, 8.38.

Synthesis of 2[Cu$_2$(6m2onic)$_3$(μ-6m2onic)(MeOH)]·[Cu$_2$(6m2onic)$_2$(μ-6m2onic)$_2$]·2[Cu(6m2onic)$_2$(MeOH)]·32H$_2$O (4$_{Cu}$). Single crystals of compound 4$_{Cu}$ were grown by following the same procedure used for compound 1$_{Mn}$ except for the use of CuCl$_2$·2H$_2$O instead of Mn(NO$_3$)$_2$·4H$_2$O. The slow evaporation of the filtered solutions gave red and green single crystals that were washed with EtOH. Yield of 45% based on metal. Anal. Calcd for C$_{116}$H$_{176}$Cu$_8$N$_{16}$O$_{84}$ (%): C, 38.20; H, 4.86; N, 6.14. Found: C, 38.15; H, 4.69; N, 6.25.

Synthesis of {[Cu(μ-6m2onic)$_2$]·6H$_2$O}$_n$ (5$_{Cu}$). Single crystals of compound 5$_{Cu}$ were obtained by following the same above mentioned procedure but in the absence of MeOH and using Cu(NO$_3$)$_2$·6H$_2$O as metal source. The slow evaporation of the filtered solutions gave light blue single crystals that were washed with MeOH. Yield of 80% based on metal. Anal. Calcd for C$_{14}$H$_{24}$CuN$_2$O$_{12}$ (%): C, 35.33; H, 5.08; N, 5.89. Found: C, 35.13; H, 5.22; N, 5.35.

Chemical characterization. Elemental analyses (C, H, N) were performed on a Leco CHNS-932 microanalyzer. IR spectra were recorded using KBr pellets in a ThermoNicolet IR 200 spectrometer in the 4000–400 cm^{-1} spectral region. Magnetic susceptibility measurements were carried out on polycrystalline samples of the complexes with a Quantum Design SQUID MPMS-7T suscepatometer at an applied magnetic field of 1000 G. The susceptibility data were corrected for the diamagnetism estimated from Pascal's Tables,[72] the temperature-independent paramagnetism, and the magnetization of the sample holder. Alternating current measurements were performed on a physical property measurement System-Quantum Design model 6000 magnetometer under a 3.5 G *ac* field and frequencies ranging from 60 to 10 000 Hz. Thermal analyses (TG/DTA) were performed on a TA Instruments SDT 2960 thermal analyzer in a synthetic air atmosphere (79% N$_2$ / 21% O$_2$) with a heating rate of 5 °C·min^{-1}. Diffuse reflectance (DR) measurements were carried out on a UV-2600 UV/vis Shimadzu spectrophotometer over polycrystalline samples of compound 2$_{Co}$. Spectra were recorded at room temperature using BaSO$_4$ as a reference material.

X-ray Diffraction Data Collection and Structure Determination. Suitable single crystals of compounds 1$_{Mn}$, 2$_{Co}$, 4$_{Cu}$ and 5$_{Cu}$ were mounted on a Bruker D8 VENTURE diffractometer equipped with area detector and graphite monochromated MoK$_\alpha$ radiation (λ = 0.71073 Å). Data collection was performed at 100(2) K on by applying the ω-scan method used for the structure determination. Data reduction was performed with the APEX2[73] software and absorption was corrected using SADABS.[74] Crystal structures were solved by intrinsic phasing using the SHELXT program[75] and refined by full-matrix least-squares on F^2 including all reflections employing the WINGX crystallographic package[76,77] or OLEX2.[78] The single crystal of compound 5$_{Cu}$ was found to be twinned, although no twin data processing was applied during the data reduction given the low percentage of the

minor component (<10%). All hydrogen atoms were located in the difference Fourier map and included as fixed contributions using riding models with isotropic thermal displacement parameters 1.2 times those of their parent atoms for the 3isoani ligand and methanol molecules, and 1.5 times in case of water molecules. The main crystallographic details and refinement data may be found in Table 7. Crystallographic data has been deposited with the Cambridge Crystallographic Data Center as supplementary publication with nos. CCDC 2159794-2159797. Copies of the data can be obtained free of charge on application to the Director, CCDC, 12 Union Road, Cambridge,

CB2 1EZ, U.K. (Fax: +44-1223-335033; e-mail: deposit@ccdc.cam.ac.uk or http://www.ccdc.cam.ac.uk).

The X-ray powder diffraction (XRPD) patterns were measured over previously grounded single crystals. For data acquisition, a Philips X'PERT powder diffractometer was used with Cu-Kα radiation (λ = 1.5418 Å) over the range 5 < 2θ < 50° with a step size of 0.026° and an acquisition time of 2.5 s per step at 25 °C. Indexation of diffraction profiles were made using FULLPROF program (pattern matching analysis)[79] on the bases of the space group and cell parameters obtained from single crystal X-ray diffraction.

Table 7. Single crystal X-ray diffraction data and structure refinement details of compounds 1_{Mn}, 2_{Co}, 4_{Cu} and 5_{Cu}.

	1_{Mn}	2_{Co}	4_{Cu}	5_{Cu}
Empirical formula	$C_{23}H_{28}MnN_3NaO_{12}$	$C_{28}H_{38}Co_2N_6Na_2O_{25}$	$C_{116}H_{176}Cu_8N_{16}O_{84}$	$C_{14}H_{24}CuN_2O_{12}$
Formula weight	616.41	1022.48	3547.13	475.89
Crystal system	monoclinic	monoclinic	monoclinic	monoclinic
Space group	$P2_1/c$	$I2/a$	$P2_1/c$	$P2_1/c$
a (Å)	14.4049(9)	13.5130(7)	20.4921(14)	5.1194(4)
b (Å)	12.2948(7)	18.4330(7)	9.4963(8)	21.9576(16)
c (Å)	15.1192(10)	15.8418(7)	37.786(2)	8.6216(6)
$β$ (°)	94.946(2)	91.342(4)	92.627(2)	98.595(3)
V (Å³)	2667.7(3)	3944.9(3)	7345.4(9)	958.27(12)
Reflections collected	6273	41953	51215	15093
Unique data/parameters	3821/ 371	5039/ 395	18810 / 1021	1683 / 134
Rint	0.1556	0.0366	0.0486	0.0827
GoF (S)[a]	1.084	1.114	1.047	1.169
R_1[b]/wR^2[c] [I>2σ(I)]	0.0559/0.0821	0.0498/0.1245	0.0625/0.1628	0.0453/0.1017
R_1[b]/wR^2[c] [all]	0.0986/0.0950	0.0551/0.1288	0.1056/0.1815	0.0613/ 0.1085

[a] $S = [\sum w(F_0^2 - F_c^2)^2 / (N_{obs} - N_{param})]^{1/2}$. [b] $R_1 = \sum ||F_0| - |F_c|| / \sum |F_0|$; [c] $wR^2 = [\sum w(F_0^2 - F_c^2)^2 / \sum wF_0^2]^{1/2}$; $w = 1/[\sigma^2(F_0^2) + (aP)^2 + bP]$ where $P = (max(F_0^2,0) + 2F_c^2)/3$ with b = 5.4554 (1_{Mn}); a = 0.0410 and b = 22.782 (2_{Co}); a = 0.0892 and b = 8.0472 (4_{Cu}); a = 0.0375 and b = 2.5559 (5_{Cu}).

Computational details. Gaussian 16 package[80] was employed for optimizing the ligand molecules (H2h6mnic and H6m2onic) as well as the excerpts of compounds 1_{Mn}, 2_{Co} and 3_{Ni} taken from X-ray structures, optimizations that were performed with DFT at the UB3LYP functional[81] with the TZV basis set for the metal atoms,[82] and the 6-31G** basis set for the rest of non-metal atoms.[83] Enthalpy energy for the ligand tautomers was performed with 6-311G++(d,p) basis set. Magnetic coupling in compounds 4_{Cu} and 5_{Cu} was analysed using broken-symmetry formalism[84,85] and also by means of CASSCF calculations (CAS (2,2) setup), using ORCA software suite in both cases (version

5.0.2).[86,87] These single point calculations were conducted with B3LYP functional[88,89] using def2-TZVP basis sets for all atoms and def2-QZVPP for the metal atoms, recontracted for zeroth-order regular approximation (ZORA) relativistic approximation.[90–93] RIJCOSX approximation with appropriate auxiliary basis sets (def2/J)[92] were employed for all calculations. *Ab initio* calculations for compounds 1_{Mn}, 2_{Co} and 3_{Ni} were also implemented in ORCA to estimate *zfs* parameters for the partially (H-optimized, in case of 1_{Mn} and 2_{Co}) or the fully (for 3_{Ni}) optimized models. Calculations with state-average complete active space self-consistent field (SA-

ARTICLE Journal Name

CASSCF) method were performed incorporating the five d-orbitals and five, seven and eight electrons for compounds **1**$_{Mn}$, **2**$_{Co}$ and **3**$_{Ni}$, respectively. One sextet, twenty four quadruplets and seventy five doublets for the Mn(II)-based, ten triplets and ten singlets for the Ni(II)-based and ten quartets and forty doublets for the Co(II)-based compounds.[63] NEVPT2 calculations were performed on SA-CASSCF converged wave functions to take in account the dynamic correlation,[94] a strategy successfully used earlier to obtain accurate estimations of the *zfs* parameters.[63,95]

Acknowledgements

Notes and references

1 M. D. Allendorf and V. Stavila, *CrystEngComm*, 2015, **17**, 229–246.

2 A. Umemura, S. Diring, S. Furukawa, H. Uehara, T. Tsuruoka and S. Kitagawa, *J. Am. Chem. Soc.*, 2011, **133**, 15506–15513.

3 M. Li, D. Li, M. O'Keeffe and O. M. Yaghi, *Chem. Rev.*, 2014, **114**, 1343–1370.

4 C. T. Chen and K. S. Suslick, *Coord. Chem. Rev.*, 1993, **128**, 293–322.

5 W. Lu, Z. Wei, Z. Y. Gu, T. F. Liu, J. Park, J. Park, J. Tian, M. Zhang, Q. Zhang, T. Gentle, M. Bosch and H. C. Zhou, *Chem. Soc. Rev.*, 2014, **43**, 5561–5593.

6 X. Liu, L. Zhang and J. Wang, *J. Mater.*, 2021, **7**, 440–459.

7 V. Guillerm, D. Kim, J. F. Eubank, R. Luebke, X. Liu, K. Adil, M. S. Lah and M. Eddaoudi, *Chem. Soc. Rev.*, 2014, **43**, 6141–6172.

8 M. Eddaoudi, D. F. Sava, J. F. Eubank, K. Adil and V. Guillerm, *Chem. Soc. Rev.*, 2015, **44**, 228–249.

9 H. Li, K. Wang, Y. Sun, C. T. Lollar, J. Li and H.-C. Zhou, *Mater. Today*, 2018, **21**, 108–121.

10 L. Jiao, J. Y. R. Seow, W. S. Skinner, Z. U. Wang and H.-L. Jiang, *Mater. Today*, 2019, **27**, 43–68.

11 J. Cepeda, S. Pérez-Yáñez, G. Beobide, O. Castillo, M. Fischer, A. Luque and P. A. Wright, *Chem. - A Eur. J.*, 2014, **20**, 1554–1568.

12 J. Rocha, L. D. Carlos, F. A. A. Paz and D. Ananias, *Chem. Soc. Rev.*, 2011, **40**, 926–940.

13 J. Heine and K. Müller-Buschbaum, *Chem. Soc. Rev.*, 2013, **42**, 9232–9242.

14 J. Cepeda and A. Rodríguez-Diéguez, *CrystEngComm*, 2016, **18**, 8556–8573.

15 A. Zabala-Lekuona, J. M. Seco and E. Colacio, *Coord. Chem. Rev.*, 2021, **441**, 213984.

16 G. Mínguez Espallargas and E. Coronado, *Chem. Soc. Rev.*, 2018, **47**, 533–557.

17 T. Yamada, K. Otsubo, R. Makiura and H. Kitagawa, *Chem. Soc. Rev.*, 2013, **42**, 6655–6669.

18 U. Huizi-Rayo, J. Gutierrez, J. M. Seco, V. Mujica, I. Diez-Perez, J. M. Ugalde, A. Tercjak, J. Cepeda and E. San Sebastian, *Nano Lett.*, 2020, **20**, 8476–8482.

19 I. Oyarzabal, B. Fernández, J. Cepeda, S. Gómez-Ruiz, A. J. Calahorro, J. M. Seco and A. Rodríguez-Diéguez, *CrystEngComm*, , DOI:10.1039/c6ce00318d.

20 A. A. García-Valdivia, J. M. Seco, J. Cepeda and A. Rodríguez-Diéguez, *Inorg. Chem.*, 2017, **56**, 13897–13912.

21 A. K. Mondal, A. Mondal and S. Konar, *Magnetochemistry*, 2020, **6**, 45.

22 J. D. Rinehart and J. R. Long, *Chem. Sci.*, 2011, **2**, 2078–2085.

23 J. J. Baldoví, E. Coronado, A. Gaita-Ariño, C. Gamer, M. Giménez-Marqués and G. Mínguez Espallargas, *Chem. – A Eur. J.*, 2014, **20**, 10695–10702.

24 S. Maheswaran, G. Chastanet, S. J. Teat, T. Mallah, R. Sessoli, W. Wernsdorfer and R. E. P. Winpenny, *Angew. Chem. Int. Ed.*, 2005, **44**, 5044–5048.

25 G. Aromí, D. Aguilà, P. Gamez, F. Luis and O. Roubeau, *Chem. Soc. Rev.*, 2012, **41**, 537–546.

26 X. L. L. Ying Wang, T. W. Wang, Y. Song and X. Z. You, *Inorg. Chem.*, 2010, **49**, 969–976.

27 D. E. Freedman, W. H. Harman, T. D. Harris, G. J. Long, C. J. Chang and J. R. Long, *J. Am. Chem. Soc.*, 2010, **132**, 1224–1225.

28 W. H. Harman, T. D. Harris, D. E. Freedman, H. Fong, A. Chang, J. D. Rinehart, A. Ozarowski, M. T. Sougrati, F. Grandjean, G. J. Long, J. R. Long and C. J. Chang, *J. Am. Chem. Soc.*, 2010, **132**, 18115–18126.

29 R. Boča, *Coord. Chem. Rev.*, 2004, **248**, 757–815.

30 A. K. Bar, C. Pichon and J. P. Sutter, *Coord. Chem. Rev.*, 2016, **308**, 346–380.

31 J. M. Frost, K. L. M. Harriman and M. Murugesu, *Chem. Sci.*, 2016, **7**, 2470–2491.

32 P. C. Bunting, M. Atanasov, E. Damgaard-Møller, M. Perfetti, I. Crassee, M. Orlita, J. Overgaard, J. Van Slageren, F. Neese and J. R. Long, *Science (80-.).*, 2018, **362**, eaat7319.

33 S. Gómez-Coca, A. Urtizberea, E. Cremades, P. J. Alonso, A. Camón, E. Ruiz and F. Luis, *Nat. Commun.*, 2014, **5**, 1–8.

34 J. Acharya, A. Swain, A. Chakraborty, V. Kumar, P. Kumar, J. F. Gonzalez, O. Cador, F. Pointillart, G. Rajaraman and V. Chandrasekhar, *Inorg. Chem.*, 2019, **58**, 10725–10735.

35 A. Sarkar, S. Dey and G. Rajaraman, *Chem. - A Eur. J.*, 2020, **26**, 14036–14058.

36 J. Nehrkorn, I. A. Valuev, M. A. Kiskin, A. S. Bogomyakov, E. A. Suturina, A. M. Sheveleva, V. I. Ovcharenko, K. Holldack, C. Herrmann, M. V Fedin, A. Schnegg and S. L. Veber, *J. Mater. Chem. C*, 2021, **9**, 9446–9452.

37 S. Güler-Kılıç and Ç. Kılıç, *J. Magn. Magn. Mater.*, 2022, **547**, 168915.

38   A. K. Mondal, A. Mondal, B. Dey and S. Konar, *Inorg. Chem.*, 2018, **57**, 9999–10008.

39   S. Adhikari, A. Sahana, B. Kumari, D. Ganguly, S. Das, P. P. Banerjee, G. Banerjee, A. Chattopadhyay, M. Fondo, J. S. Matalobos, P. Brandão, V. Félix and D. Das, *New J. Chem.*, 2016, **40**, 10378–10388.

40   Z. L. Xu, F. Y. Liu and Y. Y. Zhang, *Synth. React. Inorganic, Met. Nano-Metal Chem.*, 2014, **44**, 1504–1508.

41   B. Anacleto, P. Gomes, A. Correia-Branco, C. Silva, F. Martel and P. Brandão, *Polyhedron*, 2017, **138**, 277–286.

42   S. J. Grabowski, *Crystals*, 2021, **11**, 5.

43   S. Alvarez, D. Avnir, M. Llunell and M. Pinsky, *New J. Chem.*, 2002, **26**, 996–1009.

44   J. Cepeda and S. Pérez-Yáñez, *Eur. J. Inorg. Chem.*, , DOI:10.1002/ejic.201402269.

45   A. García-García, J. M. Méndez-Arriaga, R. Martín-Escolano, J. Cepeda, S. Gómez-Ruiz, A. Salinas-Castillo, J. M. Seco, M. Sánchez-Moreno, D. Choquesillo-Lazarte, A. B. Ruiz-Muelle, I. Fernández, C. Marín and A. Rodríguez-Diéguez, *Polyhedron*, 2020, **184**, 114570.

46   E.-Q. Gao, Y.-X. Xu and C.-H. Yan, *CrystEngComm*, 2004, **6**, 298–302.

47   S. Perez-Yanez, G. Beobide, O. Castillo, J. Cepeda, A. Luque and P. Roman, *Cryst. Growth & Des.*, 2013, **13**, 3057–3067.

48   M. Gruden-Pavlović, M. Zlatar, C. W. Schläpfer and C. Daul, *J. Mol. Struct. THEOCHEM*, 2010, **954**, 80–85.

49   M. V. Veidis, G. H. Schreiber, T. E. Gough and G. J. Palenik, *J. Am. Chem. Soc.*, 2002, **91**, 1859–1860.

50   L. Infantes and S. Motherwell, *CrystEngComm*, 2002, **4**, 454–461.

51   C. Duboc, *Chem. Soc. Rev.*, 2016, **45**, 5834–5847.

52   J. Miklovič, D. Valigura, R. Bőča and J. Titiš, *Dalt. Trans.*, 2015, **44**, 12484–12487.

53   †,‡ John Vakros, †,‡ Kyriakos Bourikas, † Spyros Perlepes, †,§ and Christos Kordulis and † Alexis Lycourghiotis*, *Langmuir*, 2004, **20**, 10542–10550.

54   N. F. Chilton, R. P. Anderson, L. D. Turner, A. Soncini and K. S. Murray, *J. Comput. Chem.*, 2013, **34**, 1164–1175.

55   M. L. Calatayud, I. Castro, J. Sletten, F. Lloret and M. Julve, *Inorganica Chim. Acta*, 2000, **300**–**302**, 846–854.

56   D. A. Pantazis, *J. Chem. Theory Comput.*, , DOI:10.1021/acs.jctc.8b00969.

57   S. Perez-Yanez, O. Castillo, J. Cepeda, J. P. Garcia-Teran, A. Luque and P. Roman, *Eur. J. Inorg. Chem.*, 2009, 3889–3899.

58   F. S. Delgado, J. Sanchiz, C. Ruiz-Pérez, F. Lloret and M. Julve, *Inorg. Chem.*, 2003, **42**, 5938–5948.

59   J. Sanchiz, Y. Rodríguez-Martín, C. Ruiz-Pérez, A. Mederos, F. Lloret and M. Julve, *New J. Chem.*, 2002, **26**, 1624–1628.

60   J.-M. Rueff, N. Masciocchi, P. Rabu, A. Sironi and A. Skoulios, *Eur. J. Inorg. Chem.*, 2001, **2001**, 2843–2848.

61   Q. Chen, J.-B. Lin, W. Xue, M.-H. Zeng and X.-M. Chen, *Inorg. Chem.*, 2011, **50**, 2321–2328.

62   F. Lloret, M. Julve, J. Cano, R. Ruiz-García and E. Pardo, *Inorganica Chim. Acta*, 2008, **361**, 3432–3445.

63   Y.-F. Deng, M. K. Singh, D. Gan, T. Xiao, Y. Wang, S. Liu, Z. Wang, Z. Ouyang, Y.-Z. Zhang and K. R. Dunbar, *Inorg. Chem.*, 2020, **59**, 7622–7630.

64   R. Herchel, L. Váhovská, I. Potočňák and Z. Trávníček, *Inorg. Chem.*, 2014, **53**, 5896–5898.

65   T. T. Da Cunha, V. M. M. Barbosa, W. X. C. Oliveira, E. F. Pedroso, D. M. A. Garciá, W. C. Nunes and C. L. M. Pereira, *Inorg. Chem.*, 2020, **59**, 12983–12987.

66   X. Q. Wei, D. Shao, C. L. Xue, X. Y. Qu, J. Chai, J. Q. Li, Y. E. Du and Y. Q. Chen, *CrystEngComm*, 2020, **22**, 5275–5279.

67   A. Rodriguez-Dieguez, S. Perez-Yanez, L. Ruiz-Rubio, J. M. Seco and J. Cepeda, *CrystEngComm*, 2017, **19**, 2229–2242.

68   K. Chattopadhyay, M. J. Heras Ojea, A. Sarkar, M. Murrie, G. Rajaraman and D. Ray, *Inorg. Chem.*, 2018, **57**, 13176–13187.

69   M. Atanasov, D. Aravena, E. Suturina, E. Bill, D. Maganas and F. Neese, *Coord. Chem. Rev.*, 2015, **289**–**290**, 177–214.

70   L. Ungur and L. F. Chibotaru, *Chem. – A Eur. J.*, 2017, **23**, 3708–3718.

71   L. F. Chibotaru and L. Ungur, *J. Chem. Phys.*, 2012, **137**, 64112.

72   A. EARNSHAW, ed. A. B. T.-I. to M. EARNSHAW, Academic Press, 1968, pp. ix–x.

73   B. A. I. Bruker Apex2, 2004.

74   G. M. Sheldrick, 1996, Program for Empirical Adsorption Correction.

75   G. M. Sheldrick, *Acta Crystallogr. Sect. A Found. Crystallogr.*, 2015, **71**, 3–8.

76   G. M. Sheldrick, *Acta Cryst.*, 2014, 3–8.

77   L. J. Farrugia, *J. Appl. Crystallogr.*, 2012, **45**, 849–854.

78   O. V Dolomanov, L. J. Bourhis, R. J. Gildea, J. A. K. Howard and H. Puschmann, *J. Appl. Crystallogr.*, 2009, **42**, 339–341.

79   J. Rodríguez-Carvajal, .

80   M. J. Frisch, G. W. Trucks, H. B. Schlegel, G. E. Scuseria, M. A. Robb, J. R. Cheeseman, G. Scalmani, V. Barone, G. A. Petersson, H. Nakatsuji, X. Li, M. Caricato, A. V Marenich, J. Bloino, B. G. Janesko, R. Gomperts, B. Mennucci, H. P. Hratchian, J. V Ortiz, A. F. Izmaylov, J. L. Sonnenberg, D. Williams-Young, F. Ding, F. Lipparini, F. Egidi, J. Goings, B. Peng, A. Petrone, T. Henderson, D. Ranasinghe, V. G. Zakrzewski, J. Gao, N. Rega, G. Zheng, W. Liang, M. Hada, M. Ehara, K. Toyota, R. Fukuda, J. Hasegawa, M. Ishida, T. Nakajima, Y. Honda, O. Kitao, H. Nakai, T. Vreven, K. Throssell, J. A. Montgomery Jr., J. E. Peralta, F. Ogliaro, M. J. Bearpark, J. J. Heyd, E. N. Brothers, K. N. Kudin, V. N. Staroverov, T. A. Keith, R. Kobayashi, J. Normand, K. Raghavachari, A. P. Rendell, J. C. Burant, S. S. Iyengar, J. Tomasi, M. Cossi, J. M. Millam, M. Klene, C. Adamo, R. Cammi, J. W. Ochterski, R. L. Martin, K. Morokuma, O. Farkas, J. B. Foresman and D. J. Fox, 2016.

81   A. D. Becke, *Phys. Rev. A*, 1988, **38**, 3098–3100.

82   A. Schäfer, H. Horn and R. Ahlrichs, *J. Chem. Phys.*, 1992, **97**, 2571–2577.

83   V. A. Rassolov, J. A. Pople, M. A. Ratner and T. L. Windus, *J. Chem. Phys.*, 1998, **109**, 1223–1229.

84   E. Ruiz, J. Cano, S. Alvarez and P. Alemany, *J. Comput. Chem.*, 1999, **20**, 1391–1400.

85   L. Noodleman, *J. Chem. Phys.*, 1981, **74**, 5737–5743.

86   F. Neese, F. Wennmohs, U. Becker and C. Riplinger, *J. Chem. Phys.*, 2020, **152**, 224108.
87   F. Neese, *WIREs Comput. Mol. Sci.*, 2012, **2**, 73–78.
88   C. Lee, W. Yang and R. G. Parr, *Phys. Rev. B*, 1988, **37**, 785–789.
89   A. D. Becke, *J. Chem. Phys.*, 1993, **98**, 5648–5652.
90   C. van Wüllen, *J. Chem. Phys.*, 1998, **109**, 392–399.
91   F. Weigend and R. Ahlrichs, *Phys. Chem. Chem. Phys.*, 2005, **7**, 3297–3305.
92   F. Weigend, *Phys. Chem. Chem. Phys.*, 2006, **8**, 1057–1065.
93   A. Hellweg, C. Hättig, S. Höfener and W. Klopper, *Theor. Chem. Acc.*, 2007, **117**, 587–597.
94   C. Angeli, S. Borini, M. Cestari and R. Cimiraglia, *J. Chem. Phys.*, 2004, **121**, 4043–4049.
95   D. Maganas, S. Sottini, P. Kyritsis, E. J. J. Groenen and F. Neese, *Inorg. Chem.*, 2011, **50**, 8741–8754.